



Analytical Prediction of Wake-Interaction Noise in Counter-Rotation Open Rotors

Arnulfo Carazo,*

Airbus Operations SAS, Toulouse, France

Michel Roger†

École Centrale de Lyon, Écully, France

& Magdi Omais‡

Airbus Operations SAS, Toulouse, France

An analytical methodology for the prediction of tonal Counter-Rotation Open Rotor wake-interaction noise is presented. Unsteady loadings on the blades are obtained from an extension of Amiet's theory for gust-airfoil interaction accounting for airfoil sweep and chord variations in the span-wise direction. The far-field sound is formulated in the frequency domain from the generic formula of acoustic dipoles rotating in a uniformly moving atmosphere, according to Ffowcs Williams & Hawkings' analogy. The expression includes the effect of dipole radial component and blade camber on noise radiation. The methodology is assessed by comparison with URANS results and wind-tunnel measurements.

I. Introduction

A Counter-Rotation Open Rotor (CROR) engine is composed of two coaxial propellers in tandem and rotating in opposite directions. Essentially for fuel-efficiency considerations, this technology is considered as a possible alternative to turbofan engines for the propulsion of future subsonic aircraft. However, CROR performance benefits are balanced by some inherent drawbacks, as the increased weight, maintenance requirements and noise emissions.

CROR noise is produced by various sources, among which the unsteadiness of the relative velocity on the rotor blades is recognized as significant. Particularly, the noise produced by the impingement of the wakes issuing from the front rotor onto the rear-rotor blades is a considerable contributor to the total noise. Tonal noise is produced by the periodic component of the oncoming disturbances while their turbulent part results in broadband noise. Whereas only the local source statistics is needed for modeling broadband noise, its phase and amplitude distribution over the blade surface is required for an accurate prediction of tonal noise, essentially because of non-compactness effects. Source distribution is dependent on the blade geometry, which explains why optimized blades can induce source destructive interferences, resulting in a reduced level of noise^{7,8}. For this reason, recent researches have been focused on providing an enhanced blade geometry representation for wake-blade interaction.

In this context, a research co-funded by Airbus Operations SAS has led to a semi-analytical methodology for CROR tonal noise prediction, aimed at providing a fast-tool for pre-design process. First considerations and specificities of blade geometry representation have been discussed in a previously reported work.⁵ The methodology is implemented in the present work and applied to a generic CROR geometry for which CFD computations and wind-tunnel measurements are available. The research presented in this paper is dedicated to tonal noise, the broadband component being discarded.

The far-field CROR tonal-noise formulation is first derived in detail in Sec. II. Only the dipole noise due to unsteady loadings is considered, the dipole radial component being included in the analysis. Unlike

*PhD Candidate. Airbus acoustic department.

†Professor. Laboratoire de Mécanique de Fluides et d'Acoustique.

‡Acoustic engineer. Airbus acoustic department.

what is done in many analytical approaches, acoustic sources are distributed over the actual mean-camber surface (MCS) of the rear-rotor blades, defined by the mean coordinates of pressure side and suction side in the direction perpendicular to the blade chord, at each radial value. The required unsteady loadings are approximated by an extension of Amiet's methodology, presented in Sec. III. Blade sweep and chord variation along the span are included as continuously varying parameters, within the scope of a strip-theory approach: the real blade-and-wake configuration is split into annular slices in which the rear-blade segment is approximated at best by a flat trapezoid. The unsteady loadings on the rear blades are deduced in the frequency domain by expanding the wake velocity defect in a Fourier series, as explained in Sec. IV, and projecting the solution back onto the MCS. The methodology is assessed in Sec. V by comparison with wind-tunnel measurements and numerical simulations.

II. Far-Field Noise Formulation

The formulation derived in this section is equivalent to a synthesis of various equations cast by D. B. Hanson, dealing with CRORs and with single propellers in forward flight. Hanson's initial approach is based on a change of variables to represent the blade motion as a translation in a helical reference frame.¹¹ Acoustic sources with zero radial dipole component are located on the helical advancing surface (ADS). An equation for CROR tonal noise is further derived with the same assumptions.⁴ Hanson & Parzych also proposed another formulation for single propellers, in which acoustic sources, including radial dipole component, can be located on any surface of reference.¹⁰ The objective of this section is to retain this level of refinement in a CROR tonal-noise formulation.

The influence of radial forces has often been discarded since their amplitude is assumed to be negligible in comparison to tangential and axial forces. However, as shown later on, radial forces radiate with the same directivity as volume displacement. Interference between both sources is then expected. Furthermore, as pointed out by Hanson, the vortex flow in a blade-tip region produces a radial suction force, the dipole radiation of which could have an important influence on noise.⁶ Also worthy of investigation, the influence of the reference surface where the equivalent acoustic dipoles are located can be studied with the formulation presented in this section. More accuracy is expected when studying blade shape influence on noise radiation.

The derivation methodology used here is different from the one used by Hanson, although the result is consistent with the aforementioned formulations. In what follows the noise radiation is first formulated assuming rotating dipoles in a quiescent medium. The effect of forward flight aligned with the rotational axis is introduced afterwards in Sec. II.C.

Consider a point dipole with arbitrary orientation rotating around a given axis, as shown in Fig. 1. Let us define two orthonormal bases, $\mathcal{B}_1 = (\mathbf{e}_x, \mathbf{e}_y, \mathbf{e}_z)$ and $\mathcal{B}_2 = (\mathbf{e}_r, \mathbf{e}_t, \mathbf{e}_x)$, associated to the global Cartesian coordinates and to the polar coordinates of the rotating dipole, respectively. The dipole path has a constant axial coordinate x_d and a constant radius R_0 . Notice that x_d is equal to zero in Fig. 1, for simplicity. The dipole force is defined by $\mathbf{F} = F_R \mathbf{e}_r + F_T \mathbf{e}_t + F_A \mathbf{e}_x$, where F_R , F_T and F_A are the radial, tangential and axial components, depicted in Fig. 1 by the red, blue and green vectors, respectively. The source-observer distance is given by $\mathbf{R}' = \mathbf{R} - \mathbf{R}_0 - \mathbf{x}_d$. All vector components are detailed in App. A.

II.A. Noise From a Rotating Dipole in a Medium at Rest

The acoustic pressure p emitted at time t' by a point dipole in subsonic motion and measured at time t at the observer Cartesian coordinates $\mathbf{x} = (x_x, x_y, x_z)$ is given by For steady loads this would be 0 right? The force is constant in radial, tangent and axial direction as the dipole spins around

$$p(\mathbf{x}, t) = \frac{1}{4\pi} \frac{\partial}{\partial x_i} \left[\frac{F_i(t')}{R'(1 - M_r)} \right] \quad (1)$$

where $M_r = \mathbf{M} \cdot \mathbf{R}' / \|\mathbf{R}'\|$ is the source Mach number in observer's direction, with $R' = \|\mathbf{R}'\|$, and where the squared brackets stand for retarded-time evaluation. This equation is reformulated here by using the common permutation rules between spatial and retarded time derivatives as This should also be 0 then for steady flow meaning that somehow the terms in the sum must get cancelled

$$p(\mathbf{x}, t) = -\frac{1}{4\pi} \left(\frac{1}{c_0} \frac{\partial}{\partial t'} \left[\frac{F_i R_i'}{R'^2(1 - M_r)} \right] + \left[\frac{F_i R_i'}{R'^3(1 - M_r)} \right] \right), \quad (2)$$

where c_0 is the sound speed in the quiescent medium. Note that no assumption has been made to derive Eq.(2), which therefore holds for geometrical near-field and far-field. Radiated noise in the near-field is a

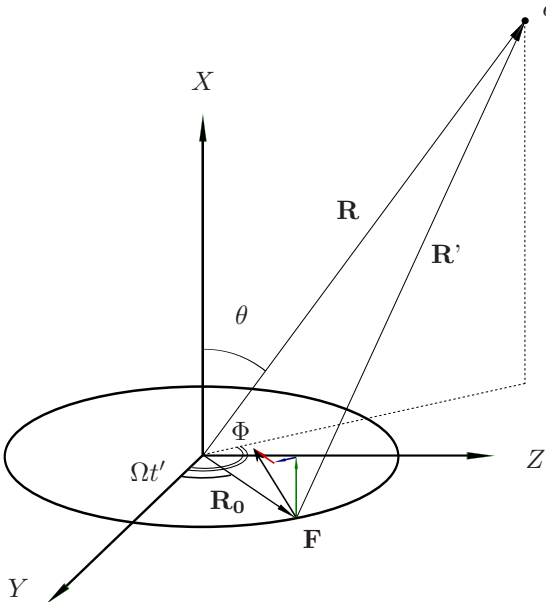


Figure 1. Rotating dipole geometry.

valuable information for predicting interior noise and structural stresses. However, in the present work, intended to provide a far-field formulation for $R \gg R_0$ and $R \gg x_d$, only the first-order approximation of the equations will be retained. For Eq.(2), this approximation is given, in the frequency domain, by:

$$\tilde{p}(\mathbf{x}, \omega) = \frac{1}{2\pi} \int_{-\infty}^{+\infty} -\frac{F_i}{1-M_r} \frac{\partial}{\partial \tau} \left(\frac{R_i'}{4\pi c_0 R^2} e^{i\omega(\tau+R'(\tau)/c_0)} \right) d\tau, \quad (3)$$

where τ is a dummy variable of integration. Developing the time derivative in Eq.(3) for the geometrical far-field approximation yields (see App. B)

I guess in this approximation Mr disappears

$$\tilde{p}(\mathbf{x}, \omega) = \frac{i\omega}{8\pi^2 c_0} \int_{-\infty}^{+\infty} \frac{\mathbf{F} \cdot \mathbf{R}'}{R^2} e^{i\omega(\tau+R'/c_0)} d\tau. \quad (4)$$

The time integral in Eq.(4) is solved by expanding the exponential on a basis of Bessel functions of the first kind, as shown in App. C. Finally, the far-field pressure radiated by a rotating point dipole reads

$$\begin{aligned} \tilde{p}(\mathbf{x}, \omega) = & \frac{i\omega e^{i\omega(R-x_d \cos \theta)/c_0}}{4\pi R c_0} \sum_{n=-\infty}^{+\infty} e^{in(\Phi-\pi/2)} \left\{ \tilde{F}_A(\omega - n\Omega) \cos \theta + \tilde{F}_T(\omega - n\Omega) \frac{nc_0}{\omega R_0} \right\} J_n \left(\frac{\omega R_0 \sin \theta}{c_0} \right) \\ & + i \sin \theta \tilde{F}_R(\omega - n\Omega) J'_n \left(\frac{\omega R_0 \sin \theta}{c_0} \right), \end{aligned} \quad (5)$$

where J_n and J'_n are the Bessel function of order n and its derivative with respect to the argument, respectively. Eq.(5) is the basis for loading noise formulation of any open rotating machine. It states that a signal of frequency ω , measured in a far-field point, can be expanded as a sum of contributions produced by force harmonics of frequencies $(\omega - n\Omega)$. This frequency modulation is a signature of the Doppler effect caused by the source circular motion and it is independent of the force frequency content. Therefore, the result holds for both tonal and broadband noise.

II.B. Source-Mode Representation

Eq.(5) states that the noise can be interpreted as an infinite sum of modes. The mode of order n has n lobes in the circumferential direction and spins around the rotation axis at the velocity $v_\varphi = \omega/(2\pi/\lambda_\varphi) = \omega/n$, where ω is the frequency in the radiated field and λ_φ is the circumferential wavelength. Intuitively, each

mode can be reproduced by a continuous circular distribution of stationary dipoles with exactly the same frequency, orientation and amplitude, but with a convenient phase lag to reproduce the mode spinning velocity and number of lobes. Two dipoles laying in this distributed source and separated from an angle α will experience a time delay $\Delta t' = \alpha/v_\varphi = n\alpha/\omega$. Hence, taking as reference the dipole located at $\alpha = 0$, the force distribution over the circle can be defined as

$$F(\alpha, t') = F\left(0, t' - \frac{n\alpha}{\omega}\right) \quad (6)$$

The expression of F is given by $F(0, t') = \tilde{A}e^{-in\omega t'}$, where \tilde{A} is the strength of the dipole distribution. The vector description of Eq.(A-1) can be used to predict the radiated noise, by replacing $(\Omega t')$ by α . Introducing these notations into Eq.(1) and expanding the exponentials in the same way as in App. C, the far-field pressure of the dipole located at α is found to be

$$\begin{aligned} \tilde{p}(\mathbf{x}, \omega)^\alpha &= \frac{i\omega e^{i\omega(R-x_d \cos\theta)/c_0}}{4\pi R c_0} e^{in\alpha} \sum_{q=-\infty}^{+\infty} e^{iq(\Phi-\pi/2-\alpha)} \left[\left\{ \tilde{A}_A(\omega - q\Omega) \cos\theta + \tilde{A}_T(\omega - q\Omega) \frac{qc_0}{\omega R_0} \right\} \right. \\ &\quad \times J_q\left(\frac{\omega R_0 \sin\theta}{c_0}\right) + i \sin\theta \tilde{A}_R(\omega - q\Omega) J'_q\left(\frac{\omega R_0 \sin\theta}{c_0}\right) \left. \right] \end{aligned} \quad (7)$$

q is doing the job of n here

where $(\tilde{A}_R, \tilde{A}_T, \tilde{A}_A)$ are the radial, tangential and axial components of \tilde{A} . The integration of this formula over α provides exactly Eq.(5), from which one identifies $2\pi\tilde{A}_i = \tilde{F}_i$. By virtue of its properties, the continuous array of phased dipoles is henceforth referred to as a **source-mode**.

II.C. Dipole Far-Field Radiation in Forward Flight

Forward flight for CROR is not the same as for the rotors I am looking at. I will have a significant amount of tangential flow

The modal structure of Eq.(5) is solely due to source rotation and is decoupled from forward-flight issues. This frequency domain approach can be extended to account for axial flight, as long as the associated Doppler effect is ignored. Such condition is fulfilled by making the observer move at the same advancing speed as the rotating dipole, so that forward flight is represented by a uniform flow opposite to the advancing direction. This corresponds to the situation encountered in wind-tunnel testing.

Is this saying that we replace a moving hub by an incoming airflow in the same direction?

The extension is made by representing each mode by a source-mode embedded in an uniform axial flow, in which the radiation is governed by the convected Green's function

$$G_c(\mathbf{x}, t/\mathbf{y}, t') = \frac{\delta(t' - t + R_e/c_0)}{4\pi R_s} \quad (8)$$

where

$$R_e = R - \frac{R_0 \sin\theta_e \cos(\Omega t' - \Phi)}{1 - M_x \cos\theta_e} - \frac{x_d \cos\theta_e}{1 - M_x \cos\theta_e}$$

and

$$R_s = R_e(1 - M_x \cos\theta_e).$$

The subscript e refers to emission polar coordinates at emission time $t' = t_e$ whereas \mathbf{y} denotes the same position in Cartesian coordinates. Using the convected Green's function and the source-mode representation of Sec. II.B, the integration over α leads to the far-field pressure radiated by an arbitrary rotating dipole, embedded in a uniform flow along $-\mathbf{e}_x$:

$$\begin{aligned} \tilde{p}(\mathbf{x}, \omega) &= \frac{i\omega e^{i\omega(R_e - \frac{x_d \cos\theta_e}{D_c})/c_0}}{4\pi R_s c_0} \sum_{n=-\infty}^{+\infty} e^{in(\Phi-\pi/2)} \left[\left\{ \tilde{F}_A(\omega - n\Omega) \frac{\cos\theta_e}{D_c} + \tilde{F}_T(\omega - n\Omega) \frac{nc_0}{\omega R_0} \right\} \right. \\ &\quad \times J_n\left(\frac{\omega R_0 \sin\theta_e}{D_c c_0}\right) + i \sin\theta_e \tilde{F}_R(\omega - n\Omega) J'_n\left(\frac{\omega R_0 \sin\theta_e}{D_c c_0}\right) \left. \right] \end{aligned} \quad (9)$$

where $D_c = 1 - M_x \cos\theta_e$.

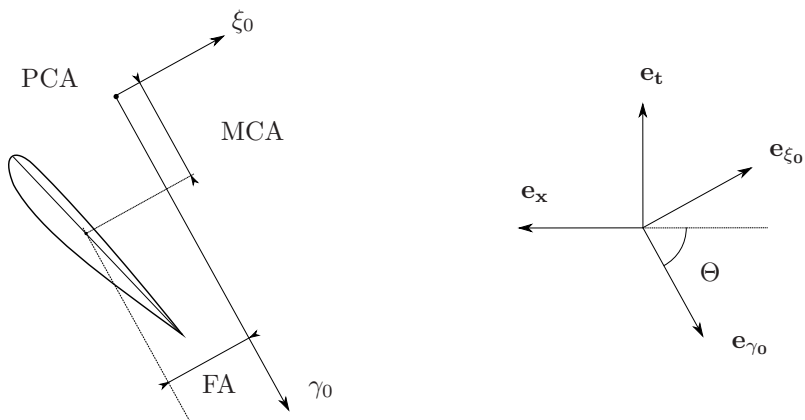


Figure 2. Advancing surface coordinate system, as defined by Hanson.⁴ The origin of the 2D reference frame is located at the Pitch-Change Axis (PCA). The blade airfoil is characterized by its Mid-Chord Alignment (MCA) in the direction γ_0 , and by its Face-Alignment (FA) in the direction ξ_0 .

II.D. General CROR Noise Formulation

CROR tonal noise specificities are now introduced in Eq.(9). The result is subsequently integrated over the blade surface of the rear-rotor, to predict its total radiation. The perturbations shed from the front-rotor are assumed to be periodic in the angular direction, which implies that rear-rotor unsteady loadings are periodic in time, with fundamental frequency $\omega_s = B_1(\Omega_1 + \Omega_2)$, where B_1 is the front-rotor blade count and (Ω_1, Ω_2) are the front-rotor and rear-rotor angular velocities, respectively. In that case, the dipole force F can be expanded into the Fourier series

$$F(t) = \sum_{k=-\infty}^{+\infty} F_k e^{-ik\omega_s t}, \text{ where } F_k = \frac{\omega_s}{2\pi} \int_0^{2\pi/\omega_s} F(t) e^{ik\omega_s t},$$

so that its Fourier transform is given by

$$\tilde{F}(\omega - n\Omega_2) = \sum_{k=-\infty}^{+\infty} F_k \delta(\omega - n\Omega_2 - k\omega_s). \quad (10)$$

From now on, let us assume that each rear-rotor blade will see the same incoming perturbation, only shifted in time and space, so the interference effect of multiple blades can be modeled by defining a phase term for the dipoles constituting a single blade. In that manner, each rear-rotor blade will be represented by a phase lag with respect to the reference blade, accounting for emission location and time effects. For a rear-rotor of B_2 blades, numbered with an index b_2 , Eq.(9) can be rewritten as⁴

$$\tilde{p} = \sum_{n=-\infty}^{+\infty} f_n \sum_{b_2=1}^{B_2} \exp \left[-i2\pi \frac{b_2}{B_2} (n + kB_1) \right] = B_2 \sum_{m=-\infty}^{+\infty} f_{mB_2-kB_1}. \quad (11)$$

Introducing Eqs.(10) and (11) in Eq.(9) and then applying an inverse Fourier transform leads to the time history of the acoustic pressure radiated by a point dipole of the rear-rotor, including radial forces and forward flight at zero incidence: Just because we put F_r in the expression, even though we don't have a clue about how to compute it.

$$\begin{aligned} p(\mathbf{x}, t) = & \frac{iB_2}{4\pi c_0 R_e D_c} \sum_{m=-\infty}^{+\infty} \sum_{k=-\infty}^{+\infty} \omega_{km} \exp \left\{ i \left[\omega_{km} \left(\frac{R_e}{c_0} - \frac{\cos \theta_e}{D_c c_0} (x_d - x_0) - t \right) + \zeta_{km} (\Phi - \pi/2 - \phi_0) \right] \right\} \\ & \times \left[\left\{ F_k^A \frac{\cos \theta_e}{D_c} + F_k^T \frac{\zeta_{km} c_0}{\omega_{km} R_0} \right\} J_{\zeta_{km}} \left(\frac{\omega_{km} R_0 \sin \theta_e}{D_c c_0} \right) + i \sin \theta_e F_k^R J'_{\zeta_{km}} \left(\frac{\omega_{km} R_0 \sin \theta_e}{D_c c_0} \right) \right] \end{aligned} \quad (12)$$

where

$$\omega_{km} = kB_1\Omega_1 + mB_2\Omega_2 \quad \text{and} \quad \zeta_{km} = mB_2 - kB_1$$

are the mode frequency and circumferential order, respectively. The coordinates (ϕ_0, x_0) stand for the dipole position at $t' = 0$. Note that this equation is qualified as a frequency-domain formulation because the field is explicitly described as a sum of modes or an equivalent combination of tones. The integration of Eq.(12) over a single rear blade surface provides the total rear-rotor acoustic radiation. For comparison with Hanson's equation,⁴ Eq.(12) can be expressed in the ADS coordinate system, though this integration can be performed numerically on any surface of reference. Let us define the advancing orthonormal basis $\mathcal{B}_3 = (\mathbf{e}_r, \mathbf{e}_{\gamma_0}, \mathbf{e}_{\xi_0})$, as depicted in Fig. 2. The dipole component projection onto this surface leads to

$$F_A = F_L \sin \Theta - F_D \cos \Theta \quad (13)$$

$$F_T = -F_L \cos \Theta - F_D \sin \Theta$$

where

$$\sin \Theta = \Omega_2 r / V_{r2} \quad \text{and} \quad \cos \Theta = V_x / V_{r2}.$$

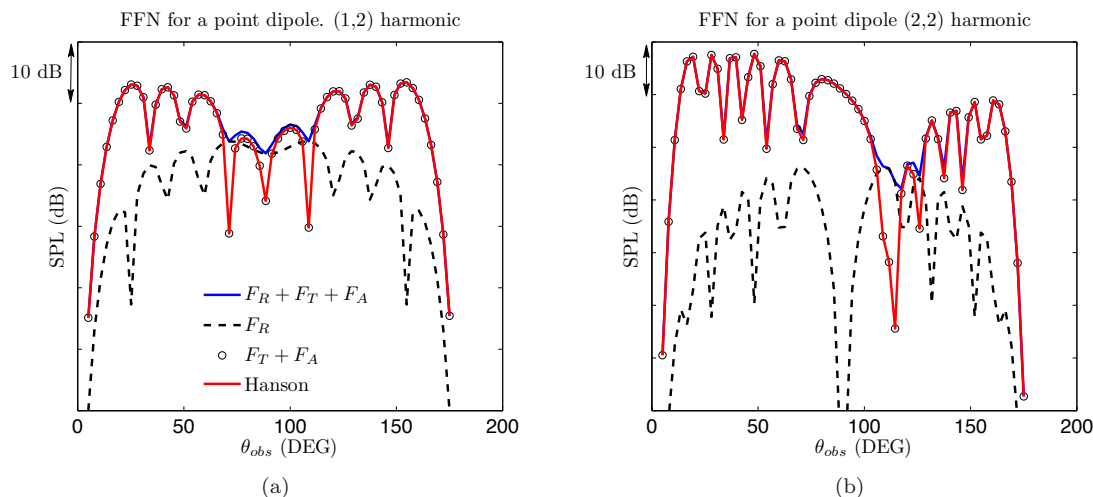


Figure 3. Far-field radiation of a rear-rotor blade point dipole, according to the reference Hanson's solution and the present formulation.

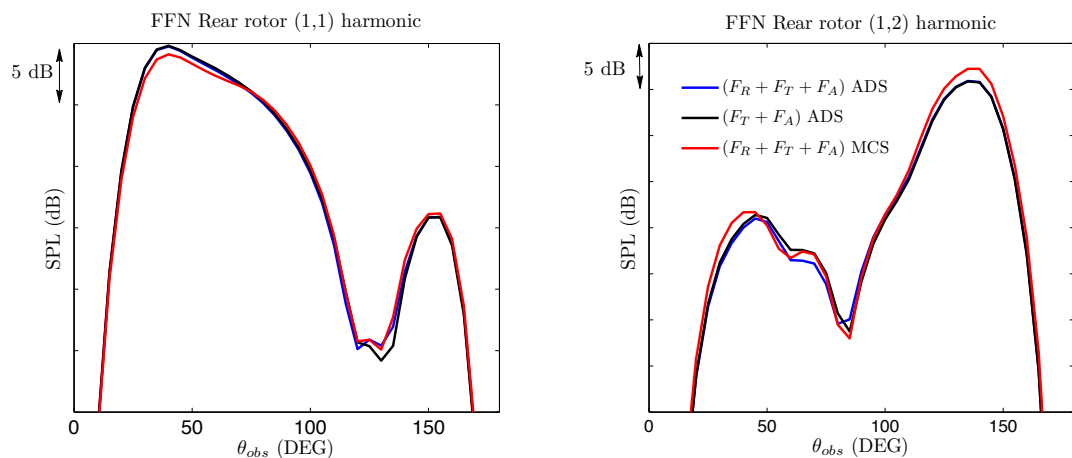


Figure 4. Typical effect of surface of reference and radial force component on directivity patterns. Black line: tangential and axial dipole components integrated on the Advancing Surface (Hanson's equation). Blue line: all dipole components integrated on the Advancing Surface. Red line: all dipole components distributed on the Mean-Camber Surface.

V_x , V_{r2} and r represent the flight velocity, the advancing velocity in the helical direction $-\gamma_0$ and the radial value, respectively. Also, in Eq.(13), F_L and F_D stand for the force components in the directions defined by $-\mathbf{e}_{\xi_0}$ and \mathbf{e}_{γ_0} . Hanson's equation is recovered with two more substitutions in Eq.(12), namely

$$x_d = -\gamma_0 \cos \Theta - \xi_0 \sin \Theta \quad \text{and} \quad \Phi = -\frac{\gamma_0 \sin \Theta}{R_0} + \frac{\xi_0 \cos \Theta}{R_0},$$

by expanding lift and drag coefficients into Fourier series and by performing analytical integration over the profile chord projection on γ_0 . An assessment of the CROR tonal noise formulation presented in this section can be achieved by considering the rear-rotor unsteady loadings as known. The determination of such information for blade-wake interactions is the subject of the subsequent sections. As a preliminary case test, the far-field noise has been computed using Eq.(12) and the original Hanson's equation for an acoustically compact cell of the rear-blade tip region of a realistic CROR geometry. The force amplitude components normalized by the axial component are $F_A = 1$, $F_T = 0.8282$ and $F_R = 0.0940$. As shown in Fig. 3, if radial component is ignored, Eq.(12) provides the same result as Hanson's equation. When the radial component is included, some differences are noticeable at localized angles, although the main trend and level are unchanged. Greater differences are expected if tip suction forces are included.

The effect of the reference surface used to represent the blade is now evaluated, for a given acoustic source. The baseline result is found by distributing the source, with its radial component being ignored, over the rear-rotor blade ADS (Hanson's original approach). Next, radial components are included on this computation to assess their effect when the source is integrated over the entire blade surface. A new computation is performed, in which the source, all components included, is distributed over the blade MCS, thought to represent better the blade geometry. In Fig. 4 is shown a comparison between these results. Differences up to 2dB are noticeable when distributing the source over different reference surfaces.

CROR far-field noise has been formulated to take into account realistic parameters as radial forces and blade camber. For practical applications, unsteady loadings on the rear rotor are still needed as input data. A semi-analytical procedure, considered as the central part of the methodology, is proposed in the next section to determine this information whenever it is unavailable from numerical simulations.

III. Rear-Rotor Unsteady Loadings Determination

III.A. Rear-Blade Geometry Representation

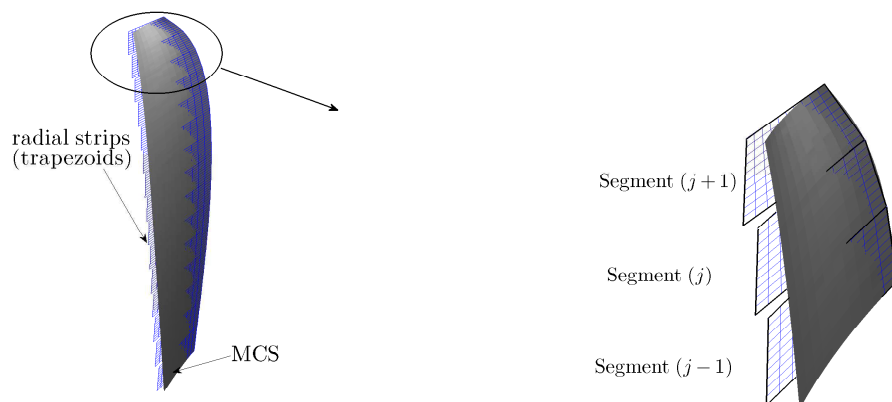


Figure 5. Rear-rotor blade MCS compared to its approximation by swept trapezoids (left). Detail of the blade tip region (right).

Unsteady loadings on the rear-rotor are determined here from an extension of Amiet's gust-airfoil interaction theory for rectangular segments. The extension allows the representation of leading-edge sweep and chord variations with span using a single formulation. Since the gust is supposed to be convected at uniform velocity, the intended application to rotating blades requires a strip-theory approach, in which each radial slice is characterized by a uniform convection velocity in unwrapped coordinates. Blade thickness, camber and angle of attack are assumed to be small so that each blade-strip surface, represented by its MCS, is approached by an equivalent flat panel for unsteady loading computation. The panel is found by projection

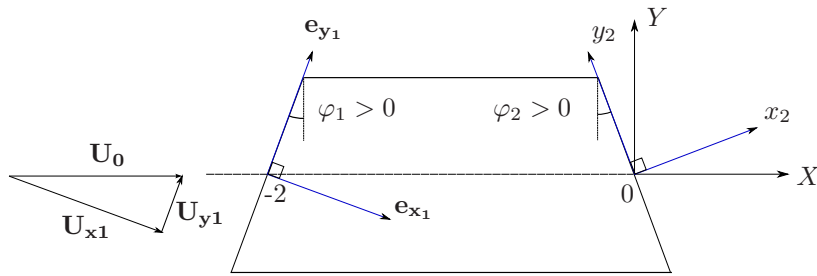


Figure 6. Trapezoid geometry for Amiet's technique extension.

of the actual unwrapped blade segment on a reference plane defined by standard least-mean-square interpolation of the leading-edge region. It is then approached by a trapezoid on the interpolation plane. This procedure is illustrated in Fig. 5.

The oncoming aerodynamic excitation is projected in the direction perpendicular to each flat trapezoidal panel and expanded in a two-dimensional Fourier series in order to define sinusoidal gusts convected at the local convection velocity. Assuming linearity, the total loading or pressure jump is given by the sum of the loadings related to each wake component. The acoustic dipoles defined by this pressure jump are then distributed back onto the blade MCS to compute its acoustic radiation, using Eq.(12). This simple procedure includes the effect of camber in the formulation by adjusting the dipole angle according to the local normal to the MCS.

III.B. Unsteady Loadings on Flat Trapezoids

A rear-blade segment features a flat trapezoid in unwrapped coordinates, with non-parallel leading and trailing edges and end-cuts parallel to the relative flow direction. Unsteady loadings due to gust-segment interaction can be determined from the formulation presented in this section. The model predicts the trace, on the segment surface, of the velocity potential scattered by the trapezoid leading-edge and its corresponding trailing-edge Kutta correction. The objective is to determine the effect of the segment shape and sweep on the unsteady loading distribution.

Let $\mathcal{B}_4 = (\mathbf{e}_{\mathbf{x}1}, \mathbf{e}_{\mathbf{y}1}, \mathbf{e}_{\mathbf{z}1})$ be a reference frame aligned with the trapezoid leading-edge, as shown in Fig. 6. The associated coordinate system (x_1, y_1) , made non-dimensional by the trapezoid half-chord at mid-span b , is defined so as to locate the trapezoid leading-edge at $x_1 = -2$. Let φ_1 and φ_2 be the sweep angles of leading-edge and trailing-edge, and $\varphi_T = \varphi_1 + \varphi_2$. The aerodynamic response of the segment leading-edge to the oncoming sinusoidal gust $W_u = \tilde{w} \exp\{i(k_{x1}x_1 + k_{y1}y_1 - \omega t)\}$ is given by Schwarzschild's theorem:¹

$$\tilde{\ell}_1(x_1, y_1) = \frac{-2\rho_0 U_{x1} \tilde{w} e^{i\pi/4}}{\sqrt{\pi(k_{x1} + \beta_{x1}^2 \kappa)(x_1 + 2)}} e^{-i(\mu M_{x1} - \kappa)(x_1 + 2)} e^{ik_{y1}y_1} e^{-i\omega t}, \quad (14)$$

where \tilde{w} and (k_{x1}, k_{y1}) are the gust amplitude and non-dimensional aerodynamic wavenumbers, ρ_0 is the mean density, U_{x1} the component of the convection velocity perpendicular to the leading edge, $M_{x1} = U_{x1}/c_0$, $\beta_{x1}^2 = 1 - M_{x1}^2$,

$$\kappa = \frac{1}{\beta_{x1}} \left[\frac{(b\omega/c_0 - k_{y1}M_{x1})^2}{\beta_{x1}^2} - k_{y1}^2 \right]^{1/2} \quad \text{and} \quad \mu = \frac{k_{x1}M_{x1}}{\beta_{x1}^2}. \quad (15)$$

ω stands here for the frequency in the reference frame of the segment. The back-scattering Kutta correction will be found again from Schwarzschild's theorem, which requires that the segment trailing-edge is defined by a single coordinate value. To fulfill this requirement, Eq.(14) must be expressed in a new reference frame aligned with the trailing-edge, with non-dimensional variables (x_2, y_2) , in which the trailing-edge is defined by $x_2 = 0$. Amiet's technique cannot be applied directly because the change of variables induces a coupling between x_2 and y_2 in the square root of Eq.(14). The issue is solved by making the reasonable assumption

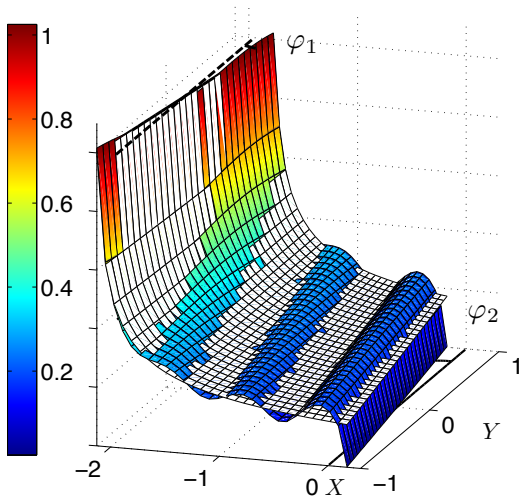


Figure 7. Sample result for a sinusoidal gust interacting with a trapezoidal segment. Unsteady lift module normalized by its value at $x_1 = -1.99$. White sheet: leading-edge term. Colored sheet: total unsteady lift corrected by the trailing-edge terms. $\varphi_1 = 10^\circ$, $\varphi_2 = 10^\circ$, aspect ratio (mid-span) $L/c = 1$, $k_c = 7.5$, convection velocity $U_0 = 150\text{m/s}$, parallel to the segment chord. Gust wavefronts perpendicular to the convection velocity.

of small aspect-ratio $\sin(\varphi_T)y_2/2 \ll 1$, which provides the following approximation for Eq.(14):

$$\tilde{\ell}_1(x_2, y_2) \approx \frac{-2\rho_0 U_{x1} \tilde{w} e^{i(a_1 x_2 + a_{20} y_2 + a_3 + \pi/4)}}{\sqrt{\pi(k_{x1} + \beta_{x1}^2 \kappa)(\cos \varphi_T x_2 + 2 \cos \varphi_1)}} \times \left[1 + \frac{e^{+i \sin \varphi_T y_2/2} - e^{-i \sin \varphi_T y_2/2}}{2i(\cos \varphi_T x_2 + 2 \cos \varphi_1)} \right], \quad (16)$$

with

$$a_1 = (k_{y1} \sin \varphi_T - B \cos \varphi_T), \quad a_{20} = (k_{y1} \cos \varphi_T + B \sin \varphi_T) \quad \text{and} \quad a_3 = 2(k_{y1} \sin \varphi_1 - B \cos \varphi_1)$$

for $B = (\mu M_{x1} - \kappa)$. In Eq.(16), the leading-edge contribution is split into three terms, each of which is characterized by a different wavenumber in the direction y_2 , namely a_{20} , $a_{2+} = a_{20} + (\sin \varphi_T)/2$ and $a_{2-} = a_{20} - (\sin \varphi_T)/2$. Amiet's methodology can now be applied independently for each of the three leading-edge contributions. For the main term, associated with a_{20} , Schwarzschild's theorem provides the following trailing-edge correction:

$$\tilde{\ell}_{20}(x_2, y_2) \approx \frac{2\rho_0 U_{x1} \tilde{w} e^{i(a_1 x_2 + a_{20} y_2 + a_3 + \pi/4)}}{\sqrt{\pi(k_{x1} + \beta_{x1}^2 \kappa)(2 \cos \varphi_1)}} \times \{1 - E^*[x_2(\hat{\kappa}_0 + A_0)]\}, \quad (17)$$

where E is the Fresnel integral defined by $E(x) = \int_0^x \frac{e^{i\xi}}{\sqrt{2\pi\xi}} d\xi$, the asterisk denoting the complex conjugate,

$$\hat{\kappa}_0 = \frac{1}{\beta_{x2}} \left[\frac{(b\omega/c_0 + a_{20}M_{y2})^2}{\beta_{x2}^2} - a_{20}^2 \right]^{1/2} \quad \text{and} \quad A_0 = a_1 + \frac{M_{x2}}{\beta_{x2}^2} (b\omega/c_0 + a_{20}M_{y2}).$$

The formulae for the other two correction terms are found by replacing a_{20} with a_{2+} or a_{2-} , and by multiplying the result by the amplitude factor $C_\pm = \pm 1/(4i \cos \varphi_1)$. The total unsteady lift on the trapezoid surface is given by $\tilde{\ell} = \tilde{\ell}_1 + \tilde{\ell}_2$, where $\tilde{\ell}_2$ is the sum of the three trailing-edge contributions. This result is a straightforward extension of a recent formulation presented for a trapezoid with leading-edge perpendicular to the convection velocity.⁵ An example of unsteady lift distribution obtained for a trapezoidal segment interacting with a skewed sinusoidal gust is depicted in Fig. 7. The comparison between the leading-edge contribution (white sheet) and the total unsteady lift (colored sheet), emphasizes how the Kutta-condition corrective terms cancel the loadings at the trailing-edge location and induce interferences in its vicinity.

III.C. Far-Field Radiation of Isolated Segments

Prior to application to a full blade, the segment shape influence on the far-field radiation has been evaluated independently for two shape parameters: leading-edge sweep and chord variation with span.⁵ In the present analysis, both parameters are included in the trapezoidal segment, the aerodynamic response of which is compared to that of a canonical rectangular panel of same chord at mid-span. Before including the effects of rotation in the acoustic field, a simpler analysis can be achieved by considering the segments as fixed in space and interacting with a uniformly convected sinusoidal gust. In that case, the segment noise radiation can be reproduced by an equivalent distribution of fixed acoustic dipoles of strength $\mathbf{F} = \tilde{\ell} dS \mathbf{e}_z$, located on the segment surface and embedded in a uniform flow. The corresponding radiation integral is computed numerically using standard quadrature (analytical derivation is still feasible in this case, but very tedious). Analytical integration is required at the leading-edge region since Eq.(14) diverges as $x_1 \rightarrow -2$. This integration is performed on parallelogram-shaped lattices aligned with the segment leading-edge and the chord-wise direction, ignoring trailing-edge correction (see next section). For fixed segments, the aeroacoustic response of each leading-edge lattice can be predicted analytically.⁵

Sweep in the segment edges modifies the dynamics of the interaction and the dipole spatial distribution. As a result, there is an inclination of the principal radiation lobe, as shown in Fig. 8. Leading-edge sweep is expected to have greater effects on noise radiation since unsteady loadings are concentrated in its vicinity. To isolate the effect of chord variation with span for a swept segment, the trapezoidal segment is compared to a parallelogram aligned to its leading-edge and with same chord at mid span. The responses of both segments to gusts parallel and oblique to their leading-edges are compared in Figs. 8(c) and 8(d). As expected, trailing-edge sweep modifies the lobes inclination in a smaller extent than leading-edge sweep, although the effect seems to be reinforced for oblique gusts.

III.D. Application to Rear-Rotor Blades

The shape effects found in the previous section can provide an insight of the effects expected when the actual shape of a rotating segment is accounted for, since rotating motion modifies only the noise propagation for a given unsteady loading distribution. The motion of each rear-rotor strip is modeled by an equivalent longitudinal motion in the helical direction, so the loadings associated with each front-rotor wake component are found using the theory presented in Sec. III.B. Far-field noise is then found using Eq.(12) for each equivalent acoustic dipole constituting the rear-rotor blade. Leading-edge dipole strengths can be found by integrating Eq.(14) on parallelogram-shaped lattices of elementary surface $\Delta S = \epsilon \Delta g$, where ϵ and Δg are the lattice span and chord. The integration on a lattice located at $x_1 = -2$ reads

$$F_{\Delta S} = A \frac{E[\epsilon D]}{\sqrt{D}} \left\{ \text{sinc}(k_{y1} \Delta g / 2) e^{ik_{y1}(y_1 + \Delta g / 2 - \tan \varphi_1)} \right\} \quad (18)$$

where $\text{sinc}(\xi)$ denotes the sine cardinal function $\sin \xi / \xi$,

$$A = \frac{-2\sqrt{2}\rho_0 U_{x1} \tilde{w} e^{i\pi/4} \Delta g}{\sqrt{\pi(k_{x1} + \beta_{x1}^2 \kappa)}} \quad \text{and} \quad D = k_{y1} \sin \varphi_1 - B \cos \varphi_1.$$

Since the interaction with a wake component is computed independently for each rear-blade strip, a source phasing is needed to correctly relate unsteady loadings on different rear-rotor segments. The required phase lag can be defined from the amount of time required by the excitation to “sweep” the leading-edge of each rear-rotor segment. Sweep velocity v_s depends on the segment inclination relative to the oncoming gust, which varies from one segment to another. Its value is given by

$$v_s = \frac{U_{x1}}{\tan \alpha_k} + U_{y1} \quad (19)$$

where α_k is the angle between the segment leading edge and aerodynamic wavefronts. The corresponding phase lag between the segment extremities is given by $\exp(-ik\omega_s l_{LE}/v_s)$, where l_{LE} is the leading-edge length. Assuming phase continuity at the blade leading-edge, the source is phased from one segment to another, from hub to tip. Once the unsteady loadings are correctly phased on the rear-rotor segments, an interpolation is performed on the segment junctions to ensure continuity of the entire source surface.

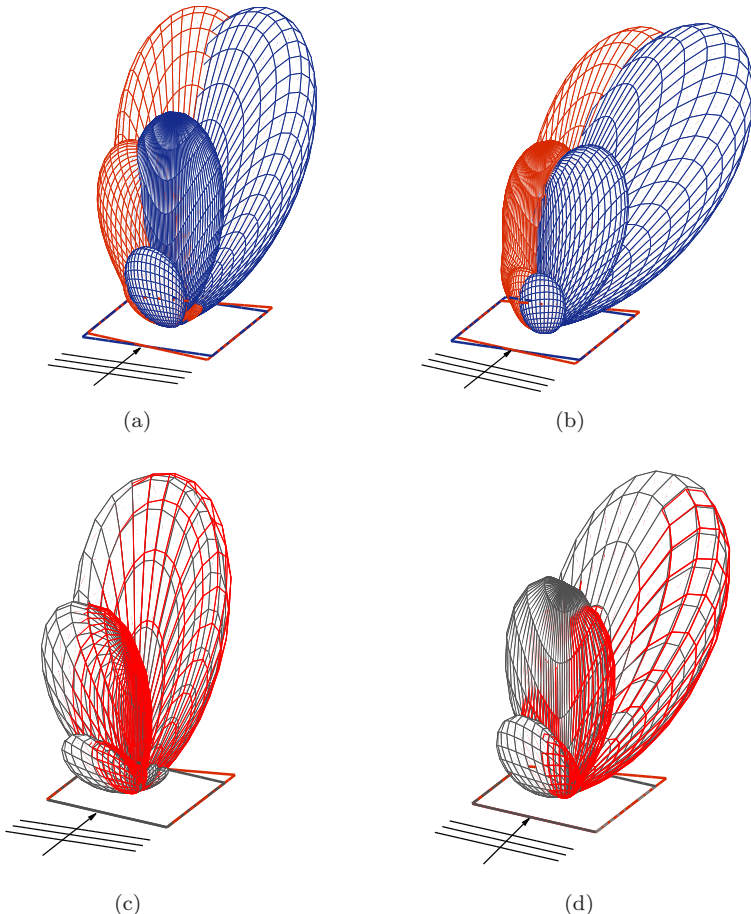


Figure 8. Effects of segment shape on far-field radiation. Upper figures: directivity lobes for a canonical rectangular segment (blue) and a trapezoidal segment, accounting for swept leading and trailing edges (red). (a) Wavefronts parallel to the rectangle leading-edge. (b) Wavefronts parallel to the trapezoid leading-edge. - Lower figures: directivity lobes for a swept parallelogram (gray) and a trapezoidal segment (red). (c) Wavefronts perpendicular to the convection velocity, as in (a). (d) Wavefronts parallel to the swept leading-edge. $\varphi_1 = 10^\circ$, $\varphi_2 = 10^\circ$, aspect ratio (mid-span) $L/c = 1$, $kc = 7.5$, $U_0 = 150\text{m/s}$.

IV. Front-Rotor Wake Representation

IV.A. Semi-Analytical Wake model

The model presented above provides the total pressure jump on a rear-blade segment, for an oncoming wake expanded in equivalent sinusoidal gusts. To perform this expansion, the perturbation must be known at the rear-rotor leading edge location, where the interaction occurs. A CFD simulation can provide this information but, once again, computational time concerns make the development of an analytical model worthy of interest. Under this perspective, a formulation of the upwash on the rear rotor is illustrated in this section. After defining the upwash due to the passage of a single blade wake, a periodization is made in the tangential direction. Finally, the excitation is expanded into sinusoidal gusts with radial and tangential wavenumbers and projected in the principal directions of the rear-rotor segments, for unsteady lift computation.

Let a front-rotor blade segment be defined by $r_1 < r < r_2$, with arbitrary sweep, lean and twist. Consider a rear-rotor segment, defined in the same radial region and approached by a flat trapezoid with arbitrary orientation. If the radial span is sufficiently short, and in analogy with a 2D cascade representation, the relative motion between these elements can be assumed as longitudinal in the tangential direction, y . The wake shed from the front element follows its chord-wise direction, which is function of r , under the assumption of slight camber and angle of attack. As a consequence, the locus of wake centerlines features an oblique surface cut by the leading edge of the rear element. An example of such a surface for a complete front-rotor blade is shown in Fig. 9(a). The corresponding excitation will sweep the rear-rotor leading edge with a

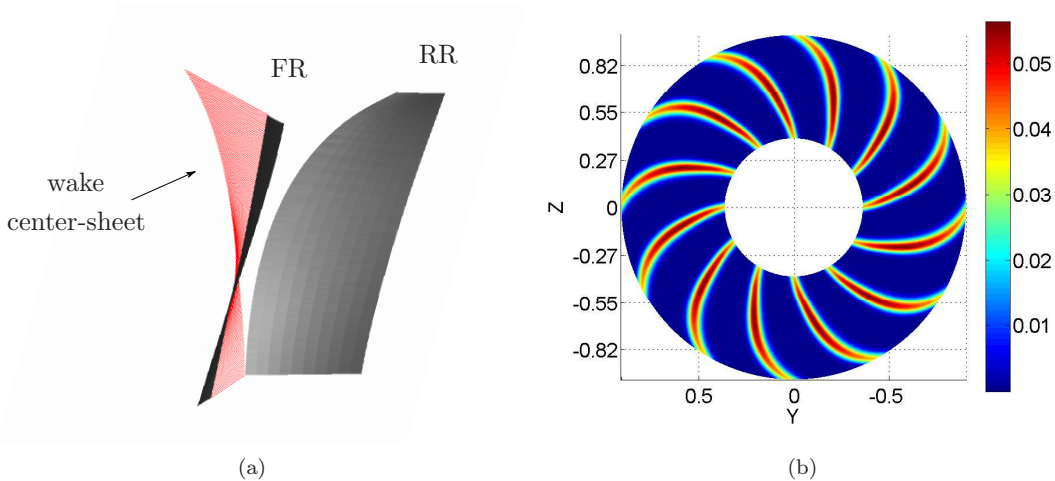


Figure 9. (a) Interaction scheme featuring one front-rotor blade and one rear-rotor blade. (b) Upwash at the leading-edge of the rear rotor, in percentage of incident velocity (front view). Coordinates normalized by rear-rotor tip radius.

finite velocity, which justifies the existence of a span-wise wavenumber. The intersection point between this surface and the leading edge of the rear-rotor segment is defined by its coordinates (y_c, r_c) . A straightforward derivation based on the methodology presented by Sears³ leads to the wake profile $U(y, r)$ for each annular region, defined as

$$\frac{U}{U_c}(y, r) = \exp \left\{ -0.693 \left(\frac{(y_c(r) - y) \cos \alpha(r)}{\delta(r)/2} \right)^2 \right\} \quad (20)$$

where $U_c(y, r)$ is the velocity defect on the wake center-sheet, $\alpha(r)$ is the angle of attack of the front element and $\delta(r)$ the semi-wake width, all parameters being function of radius. Semi-empirical rotor wake models can be used to predict δ and U_c as a function of the distance between front-rotor trailing-edge and rear-rotor leading-edge, in the wake centerline direction. The corresponding upwash becomes periodic in the tangential direction as the rear segment interacts with all the front-rotor blades. The period is defined by the mean tangential distance between two front segments, given by $y_s = \pi(r_1 + r_2)/B_1$. A radial period R_1 is necessary for the Fourier expansion in the radial direction. This value must be greater than the rear-blade radial extent, to avoid overlapping. Finally, the upwash seen by the rear-rotor $w_u(y, r)$ is given by the following Fourier series in two dimensions:

$$W_u(y, r) = \sum_{k=-\infty}^{\infty} \sum_{n=-\infty}^{\infty} \tilde{w}_{kn} e^{ik\gamma_y y} e^{ink_r r} \quad (21)$$

where $\gamma_u = 2\pi/y_s$, $k_r = 2\pi/R_1$ and where the modal amplitude \tilde{w}_{kn} is given by:

$$\tilde{w}_{kn}(y, r) = \frac{\sqrt{\pi}}{2R_1} e^{ik\gamma_y y} \int_{r1}^{r2} \frac{U_c(r) \sin \beta(r)}{K(r)} \exp \left[-\frac{\pi^2 k^2}{K(r)^2} - \frac{i2\pi k y_c(r)}{y_s} - \frac{i2\pi n r}{R_1} \right] dr. \quad (22)$$

Here $\beta(r)$ is the sum of front and rear angles of attack, and $K(r) = 2\sqrt{0.693} \cos \alpha(r) y_s / \delta(r)$. In Fig. 9(b) is shown the front-rotor wake seen at the rear-rotor leading edge of the generic geometry, obtained from Majjigi's rotor-wake model.¹⁵

IV.B. CFD Wakes as Input Data

Front-rotor wake is estimated from a semi-empirical model in Sec. IV.A. However, as most of the models available in the literature were developed for high-solidity turbofan rotors, attention must be paid to their application to CRORs. Some of these models consist in correlations between angular blade distance and semi-wake width, suggesting an inverse proportionality between both values.^{12,13} This assumption is doubtful for rotors with low blade count, for which a correlation with the profile chord is given, as an alternative, in other

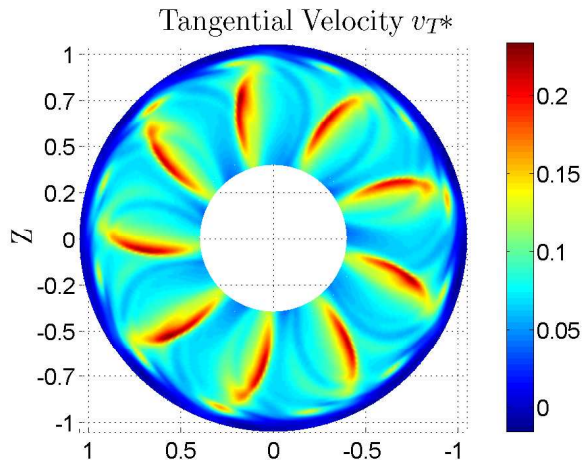


Figure 10. Extraction of CFD data. Non-dimensional tangential velocity of the particles flowing through the interpolation surface. Front view. $v_T^* = v_T \sqrt{\rho_\infty / \rho_\infty}$. Coordinates normalized by front-rotor tip radius.

models.^{14,15} Besides, some physical phenomena, intrinsic to the CROR configuration, are not taken into account by any empirical model, which increases the risk of their direct application for predicting front-rotor wakes. The main phenomena can be listed as follows:

1. It is assumed that the perturbations issued from the front rotor at a given radius will impinge the rear rotor at the same radial value, whereas a *vena contracta* effect can be caused on the cross-flow of a rotor.
2. The effect of Coriolis forces due to swirl is expected to be very dependent on blade twist and other design parameters.
3. Additional acceleration is expected from the rear-rotor thrust.
4. The influence of rear-rotor tip-vortex circulation may not be negligible.

An alternative strategy to determine the upwash at the rear-rotor leading-edge location is presented in this section. It consists in the extraction of the front-rotor wake from URANS data, assumed to account for the aforementioned phenomena. Sinusoidal gusts are then extracted using a standard Discrete Fourier-Transform (DFT) to define the input required by the blade-response model presented in Sec. III. Although the mesh grid of the available simulations does not allow to capture the whole wake harmonic content, the analysis of the lower harmonics allows physical understanding and code assessment. The velocity field can be interpolated in a reference surface close to the rear-blade leading-edge, to provide the perturbation impinging on the rear rotor. The perturbation components, given in the global Cartesian frame, (u, v, w) , are subsequently projected in radial, tangential and axial directions to enable projection on the direction normal to the rear rotor leading-edge. Fig. 10 shows the velocity tangential component of the particles flowing through the interpolation surface. As can be seen in the figure, the rear-rotor disturbances (represented by the red spots) are much more intense than the front rotor wake perturbations, merely visible in between the rear rotor bounded flow. In what follows, the main goal is to isolate front-rotor perturbations from rear-rotor bound-flow, to define the corresponding upwash needed as input in the analytical model.

The velocity field on the interpolation surface can be expressed in a reference frame bounded to the front rotor, in which front-rotor perturbations appear fixed in space while the flow related to rear rotor appears to spin at an increased angular velocity. A time integration in this reference frame provides the sum of mean front-rotor perturbations and rear-rotor mean flow in the angular domain, for each radial value. After integration, the red spots of the rear rotor are no longer noticeable and, in counterpart, front-rotor perturbations get reinforced, as seen in Fig. 11(a). Applying the same strategy for each velocity component and then projecting these values on the direction normal to the rear-rotor leading-edge, the total aerodynamic excitation acting on the rear-rotor is provided. The upwash, as shown in Fig. 11(b), is subsequently found by subtracting the mean value at each radial location to exclude rear-rotor bounded flow and mean front-rotor wake.

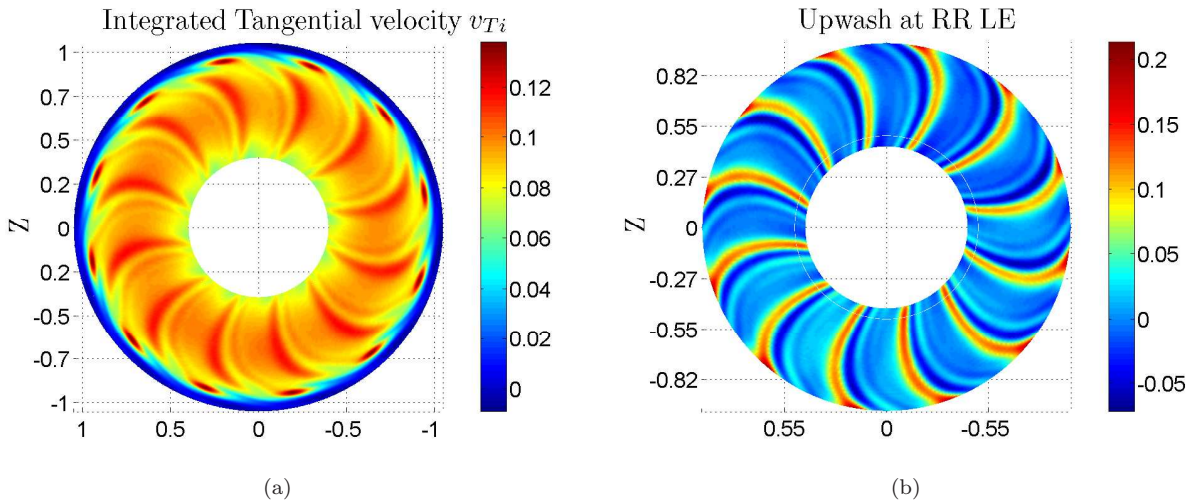


Figure 11. (a) Time integration of the perturbation tangential component, performed in the reference frame bounded to the front-rotor. Coordinates normalized by front-rotor tip radius. (b) Upwash perturbation seen at the rear-rotor leading edge. Coordinates normalized by rear-rotor tip radius.

The sinusoidal gusts required as input by the blade-response model of Sec. III can be found from the upwash DFT in two dimensions, given by

$$\tilde{w}_{num}(s, t) = \sum_{l=1}^L \sum_{m=1}^M W_{num}(l, m) e^{-i2\pi(l-1)(s-1)/L} e^{-i2\pi(m-1)(t-1)/M} \quad (23)$$

where (l, m) , (s, t) are the indices of the original and transformed matrices, respectively, and L, M the quantity of points in the tangential and radial directions, for both matrices. The subscript *num* stands for numerical results. By definition, the original information is retrieved with the associated inverse transform

$$W_{num}(l, m) = \frac{1}{LM} \sum_{s=1}^L \sum_{t=1}^M \tilde{w}_{num}(s, t) e^{i2\pi(l-1)(s-1)/L} e^{i2\pi(m-1)(t-1)/M}. \quad (24)$$

Eq.(24) can be expressed as a discrete sum of sinusoidal gusts, defined for spacial variables. For instance, in the angular direction can be defined the variable

$$\theta = (l - 1)\Delta\theta = (l - 1)\frac{\theta_{max} - \theta_{min}}{L}, \quad (25)$$

where θ_{max} and θ_{min} are the angular domain limits and $\Delta\theta$ represents the grid spacing, assumed to be regular. Any pattern in the angular direction will be expanded in sinusoidal components for which the domain length must be multiple of the wavelength. This consideration leads to the angular wavenumber

$$\kappa_\theta = \frac{2\pi}{\lambda_s} = \frac{2\pi(s - 1)}{\theta_{max} - \theta_{min}} = (s - 1)\gamma_\theta. \quad (26)$$

The same reasoning in the radial direction leads to the equivalent radial wavenumber

$$\kappa_r = \frac{2\pi(t - 1)}{r_{max} - r_{min}} = (t - 1)k_r, \quad (27)$$

which allows to write Eq.(24) as :

$$W_{num}(\theta, r) = \sum_{k=-\frac{L}{2}-1}^{\frac{L}{2}-1} \sum_{n=-\frac{M}{2}-1}^{\frac{M}{2}-1} \hat{w}_{kn} e^{ik\gamma_\theta\theta} e^{ink_r r} \quad (28)$$

where $k = s - 1$, $n = t - 1$ and $\hat{w}_{kn} = \tilde{w}_{num}(k, n)/LM$. For a sufficiently high number of grid points, this equation is identified with Eq.(21), with $y = \theta r$ and $\gamma_\theta = \gamma_y r$. The perturbation upwash has been expanded

in sinusoidal gusts and then synthesized using only the five first front-rotor harmonics, as a simple check for the procedure. The comparison between both data is shown in Fig. 12.

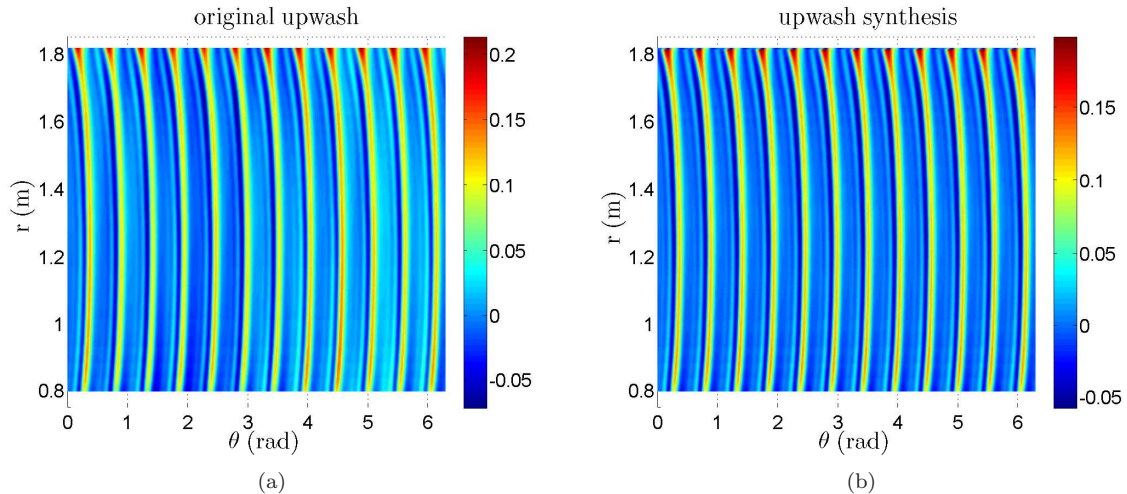


Figure 12. (a) Excitation upwash in (θ, r) coordinates. (b) Upwash synthesis using the first five front-rotor harmonics.

V. Methodology Assessment

The noise prediction method has been presented as a chain of successive transfer functions, each of which accounts for a physical aspect from front-rotor wake generation to acoustic pressure radiation. This approach allows assessing each transfer function independently, by comparison of the responses provided by both the tested function and an appropriate reference method, to the same input. In this perspective, the blade-response model presented in this paper is tested against numerical simulations. The main idea is to post-process CFD data to extract an input to the blade-response model and then to compare the blade response provided by the model to the computed one. A Fourier Transform of the resulting time-dependent pressure jump is then performed to handle a frequency domain comparison. Subsequently, the acoustic field is computed using the far-field radiation formula presented in Sec. II. The results are finally compared to their CFD/CAA counterparts and to available wind tunnel test (WTT) results.⁹

The unsteady rear-blade pressure-jump spectrum presents localized peaks at the frequencies $k\omega_s$. The loading distribution obtained for a given value of k is responsible for noise radiation at frequencies ω_{km} , as explained in II.D. Analytical prediction of the loading mode k is obtained by adding the loading obtained for each wake component inducing the frequency $k\omega_s$. Wake components inducing the same frequency can be gathered on a single excitation defined from Eq.(21) by $W_u^k = \sum_{n=-\infty}^{\infty} \tilde{w}_{kn} e^{ik\gamma_y y} e^{ink_r r}$. In that manner, the first-order blade pressure distribution is found by feeding the blade-response model with the excitation defined by W_u^1 . Analytical blade response to a CFD wake, post-processed as explained in IV.B, is assessed by the numerical pressure jump extracted from the same simulation. In Fig. 13 is shown such a comparison, for the first loading mode ($k = 1$). Differences in loading distribution are noticeable in the tip region where tip-vortex contamination is significant. However, a rather good agreement is found in terms of amplitude and phase distribution over the blade surface.

Finally, a comparison of the corresponding acoustic directivities with WTT and CFD/CAA results is shown in Fig 13. Although the directivity patterns are relatively consistent with existing data, an over prediction of the acoustic levels by up to 20dB at some particular angles is noticed. The reasons for these discrepancies have not yet been identified and are still under investigation. It must be noted that some key features of the numerical description of the pressure jump at the leading-edge differ significantly from the analytical solution.

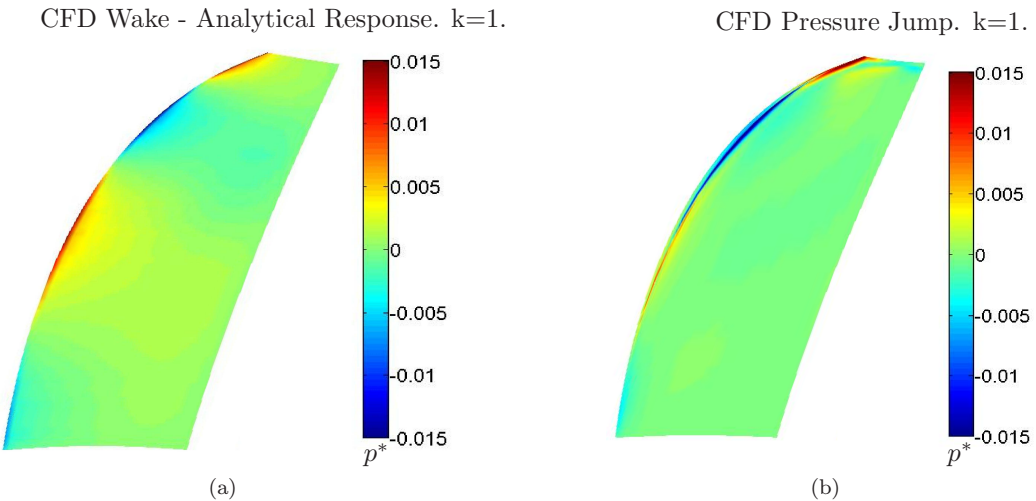


Figure 13. Real part of the pressure jump normalized by the static pressure in free stream. $p^* = p/p_\infty$. (a) CFD wake extracted in the vicinity of rear-rotor leading-edge, unsteady loadings from Amiet's theory for trapezoidal segments. (b) Fourier transform of CFD pressure jump.

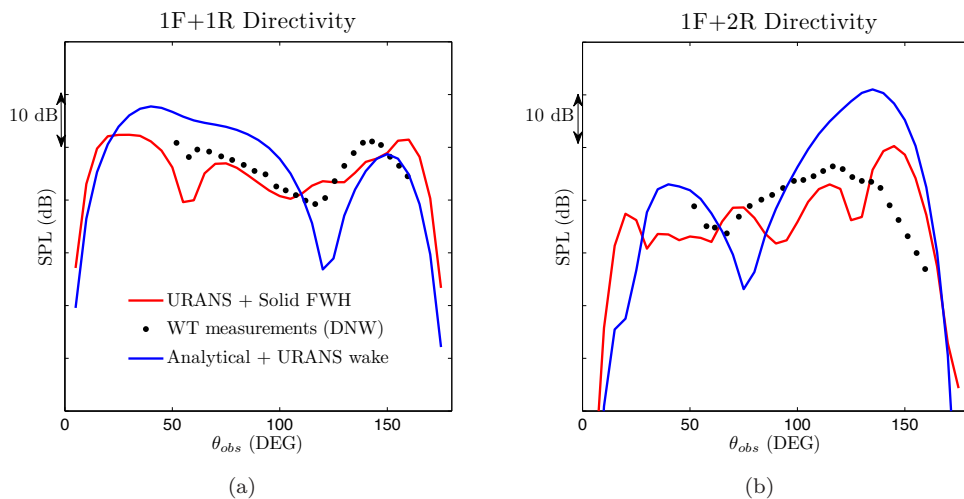


Figure 14. Methodology assessment by comparison with wind-tunnel measurements (DNW).⁹ (a) Directivity for the harmonic 1F+1R. Comparison between wind-tunnel measurements, numerical computation and analytical method. PRELIMINARY RESULTS. (b) Idem for the harmonic 1F+2R.

VI. Conclusion

A semi-analytical methodology for CROR tonal noise prediction has been presented. A far-field radiation model is derived from the formulation of a rotating acoustic dipole embedded in a uniform flow. It includes the contribution of the radial dipole component and the effect of rear-rotor blade camber on noise radiation. The unsteady blade loadings are obtained from an extension of Amiet's methodology for gust-airfoil interaction accounting for blade sweep and chord variation with span, introduced as continuous parameters. The required front-rotor wake can be deduced from semi-empirical models or extracted from numerical simulations. The methodology has been assessed by comparison to numerical simulations and wind-tunnel measurements on a generic geometry. The analytical aerodynamic response seems to correctly predict the main features of the unsteady loadings on the rear-blade surface as far as they are due to viscous wake interaction. Yet the predicted far-field noise directivity patterns still exhibit some discrepancies with wind-tunnel measurements and numerical simulations available from previous investigations. Essentially, the overall acoustic levels remain over predicted at some observer locations. Even though the present analytical modeling is still at a preliminary step, the discrepancies are more likely attributed to the fine features of the induced unsteady lift on the blades. This point will be matter to further investigations and eventual ways of improvement.

Acknowledgments

The authors wish to thank Airbus acoustic numerical methods group for providing the CFD/CAA data used in this study. They also acknowledge Rolls-Royce for the fruitful collaboration in the framework of the test campaign referred to in this paper.

VII. APPENDIX

A. Rotating Dipole Vector Representation

The observer position, radial direction and dipole force are defined by the following vectors in the Cartesian basis \mathcal{B}_1 :

$$\begin{array}{c|ccc} \mathbf{R} & R \cos \theta & \mathbf{R}_0 & 0 \\ & R \sin \theta \cos \Phi & \mathcal{B}_1 & R_0 \cos \Omega t' \\ \mathcal{B}_1 & R \sin \theta \sin \Phi & & R_0 \sin \Omega t' \end{array} \quad \begin{array}{c|cc} \mathbf{F} & F_A \\ & -F_T \sin \Omega t' + F_R \cos \Omega t' \\ \mathcal{B}_1 & F_T \cos \Omega t' + F_R \sin \Omega t' \end{array} \quad (\text{A-1})$$

where $R = \|\mathbf{R}\|$. Using these expressions, the source-observer distance \mathbf{R}' is given by the difference $\mathbf{R}' = \mathbf{R} - \mathbf{R}_0 - \mathbf{x}_d$, which leads to

$$\begin{array}{c|cc} \mathbf{R}' & R \cos \theta - x_d & \partial \mathbf{R}' / \partial t' \\ & R \sin \theta \cos \Phi - R_0 \cos \Omega t' & \mathcal{B}_1 \\ \mathcal{B}_1 & R \sin \theta \sin \Phi - R_0 \sin \Omega t' & 0 \\ & & \Omega R_0 \sin \Omega t' \\ & & -\Omega R_0 \cos \Omega t' \end{array} \quad (\text{A-2})$$

From Eqs. A-1 and A-2

$$\mathbf{F} \cdot \mathbf{R}' = R[F_A \cos \theta - F_T \sin \theta \sin(\Omega t' - \Phi) + F_R \sin \theta \cos(\Omega t' - \Phi)] - F_A x_d - F_R R_0 \quad (\text{A-3})$$

$$R' = \|\mathbf{R}'\| = R \left(1 + \frac{R_0^2}{R^2} - \frac{2R_0}{R} \sin \theta \cos(\Omega t' - \Phi) - \frac{2x_d \cos \theta}{R} + \frac{x_d^2}{R^2} \right)^{1/2} \quad (\text{A-4})$$

B. Far-Field Approximation

The far-field approximation of Eqs. A-3 and A-4, is obtained by retaining only the first order terms for $R \gg R_0$ and $R \gg x_d$. This leads to:

$$\mathbf{F} \cdot \mathbf{R}' \approx R[F_A \cos \theta - F_T \sin \theta \sin(\Omega \tau - \Phi) + F_R \sin \theta \cos(\Omega \tau - \Phi)], \quad (\text{A-5})$$

$$R' \approx R - R_0 \sin \theta \cos(\Omega \tau - \Phi) - x_d \cos \theta, \quad (\text{A-6})$$

$$\frac{1}{R'} \approx \frac{1}{R}. \quad (\text{A-7})$$

Developing the retarded time derivative of Eq.(3), and including Eqs.(A-5), (A-6) and (A-7) provides:

$$\begin{aligned} \tilde{p}(\mathbf{x}, \omega) = & \frac{1}{2\pi} \int_{-\infty}^{+\infty} \frac{F_i R_i}{4\pi c_0 R^2} \left\{ i\omega + \frac{2Mr}{(1-M_r)R} \right\} e^{i\omega(\tau+R'/c_0)} d\tau \\ & + \frac{1}{2\pi} \int_{-\infty}^{+\infty} \frac{\Omega F_T R_0}{4\pi c_0 (1-M_r) R^2} e^{i\omega(\tau+R'/c_0)} d\tau \end{aligned} \quad (\text{A-8})$$

The second integral in Eq.(A-8) is a second order term, and is then discarded in this analysis. Only the first term in the first integral bracket is retained. The result leads directly to Eq.(4).

C. Derivation of Rotating Dipole Formula

Let us define each dipole force component as an inverse Fourier transform, by

$$F_i(\tau) = \int_{-\infty}^{+\infty} \tilde{F}_i(\bar{\omega}) e^{-i\bar{\omega}\tau} d\bar{\omega}.$$

By introducing the notations $a = \omega R_0 \sin \theta / c_0$, $b = (\bar{\omega} - \omega) / \Omega$ and $\xi = \Omega\tau - \Phi$, and with appropriate factorization, Eq.(4) can be expressed as

$$\tilde{p}(\mathbf{x}, \omega) = \frac{i\omega e^{i\omega(R-x_d \cos \theta)/c_0}}{8\pi^2 R c_0} \int_{-\infty}^{+\infty} [\tilde{F}_A \cos \theta(I_1) - \tilde{F}_T \sin \theta(I_2) + \tilde{F}_R \sin \theta(I_3)] d\bar{\omega} \quad (\text{A-9})$$

where

$$\begin{aligned} I_1 &= \int_{-\infty}^{+\infty} e^{-i[b(\Phi+\xi)-a \cos \xi]} d\xi \\ I_2 &= \int_{-\infty}^{+\infty} \sin \xi e^{-i[b(\Phi+\xi)-a \cos \xi]} d\xi \\ I_3 &= \int_{-\infty}^{+\infty} \cos \xi e^{-i[b(\Phi+\xi)-a \cos \xi]} d\xi. \end{aligned}$$

The evaluation of the retarded time integrals in Eq.(A-9) is carried out by using the following identity:

$$e^{-ia \cos \xi} = \sum_{n=-\infty}^{\infty} (-i)^n J_n(a) e^{-in\xi}. \quad (\text{A-10})$$

In that way, I_1 is developed as

$$\begin{aligned} I_1 &= e^{-ib\Phi} \sum_{n=-\infty}^{+\infty} (-i)^n J_n(a) \int_{-\infty}^{+\infty} e^{-i\xi(b-n)} \\ &= 2\pi\delta(b-n)e^{-ib\Phi} \sum_{n=-\infty}^{+\infty} (-i)^n J_n(a) \end{aligned} \quad (\text{A-11})$$

The same technique is applied to solve I_2 and I_3 . Here, the derivatives of A-10 with respect to ξ and then to a , lead to

$$I_2 = 2\pi\delta(b-n)e^{-ib\Phi} \frac{n}{a} \sum_{n=-\infty}^{+\infty} (-i)^n J'_n(a) \quad (\text{A-12})$$

$$I_3 = i2\pi\delta(b-n)e^{-ib\Phi} \sum_{n=-\infty}^{+\infty} (-i)^n J'_n(a) \quad (\text{A-13})$$

where $J'_n(a)$ is the Bessel function derivative with respect to its argument. Eq.(5) is found by expressing these results in the main text notations and by using the properties of the Dirac delta function to solve the integral over $\bar{\omega}$.

References

- ¹Amiet R. K., "High Frequency Thin-airfoil Theory for Subsonic Flow", AIAA Journal, vol 14(8). p 1076-1082.
- ²Adamczyk J. J., "The Passage of an Infinite Swept Airfoil through an Oblique Gust", NASA Contractor Report, NASA CR-2395, May. 1974.
- ³Sears W. R. and Kemp H. N., "The Unsteady Forces Due to Viscous Wakes in Turbomachines", Journal of Aeronautical Sciences, N 22, 1955.
- ⁴Hanson, D. B., "Noise of Counter-rotation Propellers", Journal of Aircraft, Vol 22 N7 p609-617, July 1985.
- ⁵Roger M. and Carazo A., "Blade-Geometry Considerations in Analytical Gust-Airfoil Interaction Noise Models", 16th AIAA/CEAS Aeroacoustics Conference. No AIAA 2010-3799. Sotockholm, June 2010.

⁶Hanson, D. B., "Propeller Noise Caused by Blade Tip Radial Forces", AIAA-86-1892, AIAA 10th Aeroacoustics Conference, Seattle, Washington. 1986.

⁷Envia, E. and Nallasamy M., "Design Selection and Analysis of a Swept and Leaned Stator Concept", Journal of Sound and Vibration, 228(4). 1999.

⁸Hanson, D. B., "Influence of Propeller Design Parameters on Far-Field Harmonic Noise in Forward Flight", AIAA Journal, Vol 18 N11 pp 1313-1319, November 1980.

⁹Ricouard J., Julliard E., Omais M. and Regnier V. "Installation effects on Contra-Rotating Open Rotors", 16th AIAA/CEAS Aeroacoustics Conference. No AIAA 2010-3795. Sotockholm, June 2010.

¹⁰Hanson D. B., Parzych D. J., "Theory for Noise of Propellers in Angular Inflow With Parametric Studies and Experimental Verification", NASA Contractor Report, NASA CR-4499, March. 1993.

¹¹Hanson, D. B., "Helicoidal Surface Theory for Harmonic Noise of Propellers in the Far Field", AIAA Journal, Vol 18 N 10 p1213-1220, October 1980.

¹²Philbrick D.A., Topol D.A. "Development of a Fan Noise Design System. Part 1: System Design and Source Modeling", 15th AIAA Aeroacoustics Conference. No AIAA-93-4415. Long Beach, CA 1993.

¹³Raj R., Lakhminarayana B. "Three Dimensional Characteristics of Turbulent Wakes behind Rotors of Axial Flow Turbomachinery", Transcriptions of the ASME, April 1976.

¹⁴Reynolds B., Lakhminarayana B. "Characteristics of Lightly Loaded Fan Rotor Blade Wakes", NASA CR-3188, 1979.

¹⁵Majjigi R.K. and Gliebe P.R. "Development of a Rotor Wake/Vortex model", NASA-CR 174849.